Fractal Growth Phenomena

Tamás Vicsek

Institute for Technical Physics
Budapest, Hungary

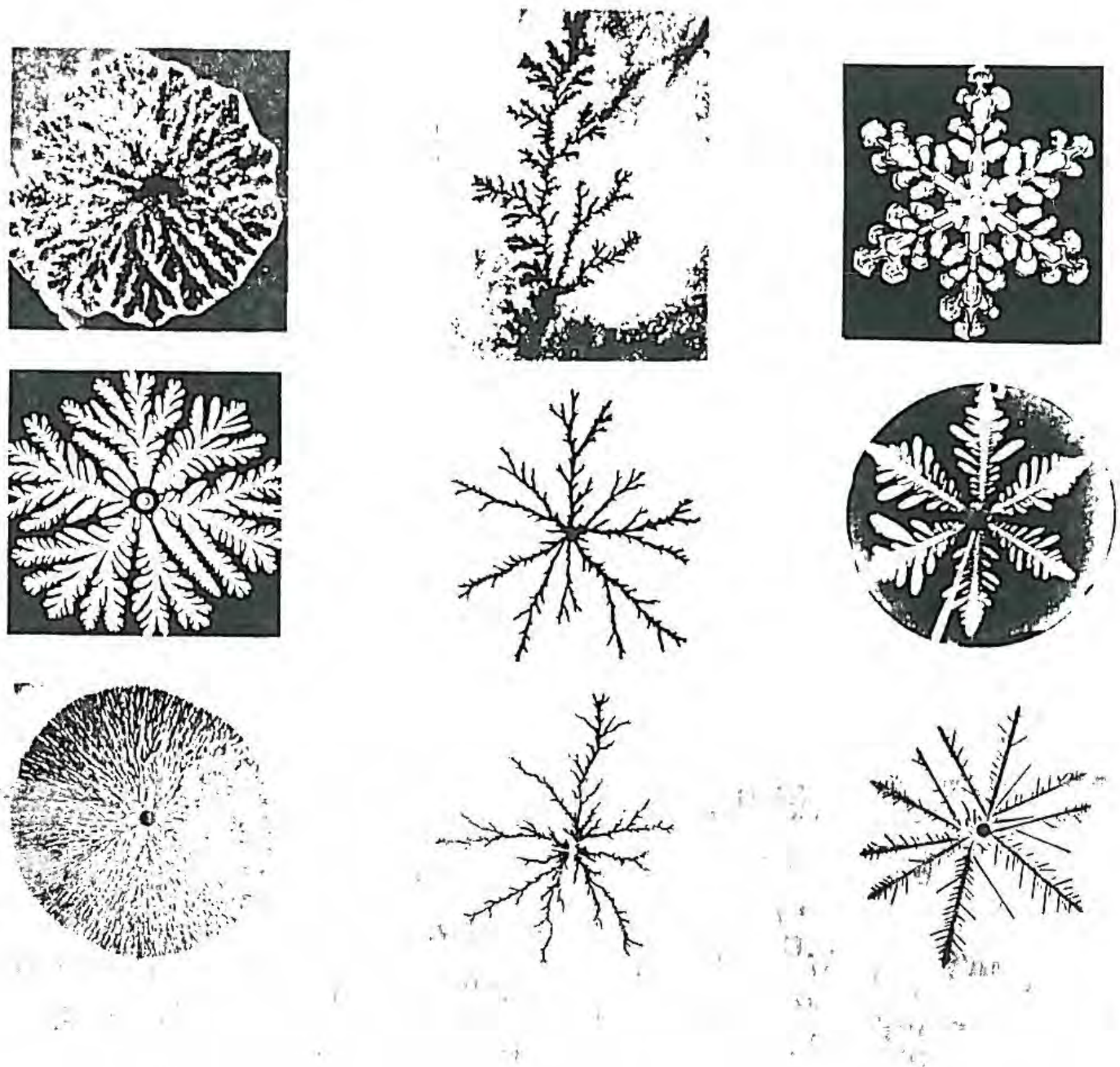

WORLD SCIENTIFIC
Singapore

$D = A \cdot b^{\alpha}$

$C(r) \sim A r^{\alpha} \quad r \to br \quad C(br) \sim D r^{\alpha}$

Scaling, new-analitikus, kritikus viselkedés, kritikus pont univerzális

kritikus exponensek

Part III

FRACTAL PATTERN FORMATION

Chapter 10.

EXPERIMENTS ON LAPLACIAN GROWTH

The large number of relevant new results obtained by various theoretical approaches and computer simulations has stimulated an increased interest in the experimental systems exhibiting fractal pattern formation. It has turned out that there are many publications and unpublished results on the desks of scientists which, in the light of the recent theoretical progress, may represent good starting points for further investigations. In particular, the formation of random branching structures in thin solid films was observed some time ago in several laboratories, but it was the theoretical framework of fractal geometry which revived the interest in the related experiments.

The majority of the latest experiments, however, have been designed to produce data for additional theoretical research and to check the validity of various predictions. The most suitable systems to carry out this kind of investigation are those in which the behaviour of the growing interface is determined by a relatively small number of well defined parameters. Viscous fingering in the nearly two-dimensional Hele-Shaw cell is a good example for such processes. The related results will be discussed at the beginning of this chapter. The most studied further phenomena leading to complex interfacial patterns are solidification and electrodeposition which will be treated in

separate Sections. Finally, a few more types of experiments will be reviewed.

As we shall see, in the above mentioned experiments the motion of the interface is dominated by a quantity which in various approximations satisfies the Laplace equation. They also share the property of being relevant from the point of view of *applications*. For example, viscous fingering plays an essential role in the process of secondary oil recovery, where water is pumped into the ground through a well to force the oil to flow closer to the neighbouring wells. Furthermore, the formation of dendritic structures during solidification determines the final internal texture of many alloys, in this way strongly influencing their mechanical and other properties.

10.1. VISCOUS FINGERING

The phenomenon of viscous fingering takes place when a less viscous fluid is injected into a more viscous one under circumstances leading to a fingered interface. In general, the motion of the two fluids and the interface between them is described by the Navier-Stokes equation, which is a non-linear equation containing terms depending on such factors as the gravitation, heat diffusion or shear viscosity. Here we shall discuss experiments where the conditions are such that most of the terms in the Navier-Stokes equation can be neglected and the resulting mathematical problem corresponds to Laplacian growth (Bensimon *et al* 1986).

If the fluids are embedded in a porous medium, it is the term related to viscous forces which dominates the flow. In such media the fluid flows through narrow channels and its velocity is limited by the walls of the channels. A similar effect occurs in the case of quasi-two-dimensional flows without the presence of a porous medium, where instead of narrow channels the flow is confined to a thin layer between two closely placed plates.

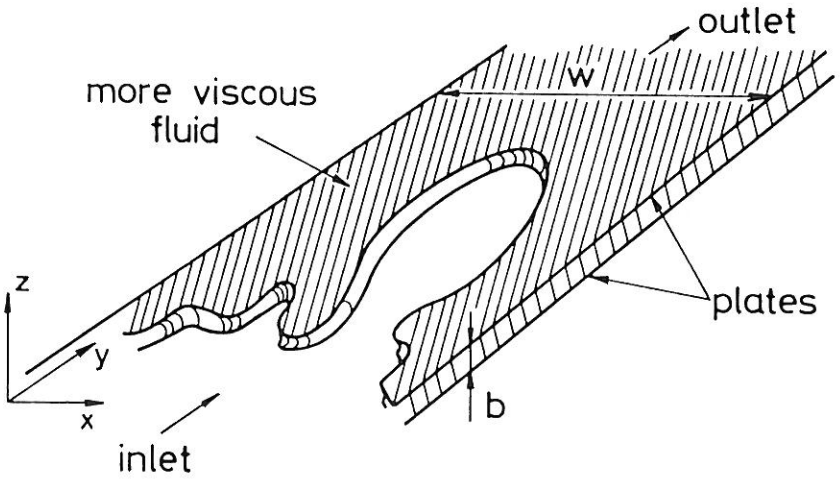

Figure 10.1. Schematic representation of the longitudinal Hele-Shaw cell. Unstable, finger-like patterns are observed if the less viscous fluid is injected into the more viscous one.

10.1.1. The Hele-Shaw cell

At the end of the last century Hele-Shaw (1898) introduced a simple system to study the flow of water around various objects for low Reynolds numbers. The cell he designed consists of two transparent plates of linear size w separated by a relatively small distance b (typical sizes are in the region $w \sim 30$ cm and $b \sim 1$ mm). The viscous fluids are placed between the plates and pressure can be applied either at one of the edges (longitudinal version, Fig. 10.1) or at the centre of the upper plate (radial version) of the cell. In Appendix B more details are given, together with a few useful suggestions for those who are interested in building a simple Hele-Shaw cell. Clearly, the Hele-Shaw cell in its above described form is suitable for the investigation of two-dimensional flows, and correspondingly, most of the results concerning fractal viscous fingering have been obtained for $d = 2$.

The relation of viscous fingering to Laplacian growth can be shown by asssuming that the plates are horizontal, and the flow in the x, y plane has a velocity profile $v(z) = [v_x^2(z) + v_y^2(z)]^{1/2}$ which is approximately parabolic in the direction z perpendicular to the plates

$$v(z) = a(b^2/4 - z^2). \tag{10.1}$$

Furthermore, we assume that $v_z = 0$ and $\partial v_x/\partial x = \partial v_y/\partial y = 0$. For the average velocity one has

$$\bar{v}(z) = \frac{1}{b}\int_{-b/2}^{b/2} v(z) = \frac{ab^2}{6}. \tag{10.2}$$

If the gravitational effects can be neglected the Navier-Stokes equation has the form

$$\nabla p = \mu \nabla^2 \vec{v} + \rho \partial \vec{v}/\partial t, \tag{10.3}$$

where μ is the viscosity of the fluid, ρ is its density, and p denotes the pressure. For small b the first term of the right-hand side in (10.3) dominates, because it is proportional to $1/b^2$. Inserting (10.1) into (10.3) (where the second term of the right-hand side is neglected) and using (10.2) we get

$$\vec{v} = -\frac{b^2}{12\mu_i}\nabla p, \tag{10.4}$$

The above equation represents the so called Darcy's law expressing the fact that for small b the average velocity is proportional to the local force. Assuming that the fluids are incompressible one arrives at the Laplace equation $\nabla^2 p = 0$ (9.1) for the pressure distribution p, from the condition that the divergence of the velocity vanishes. The boundary condition (9.2) is essentially equivalent to (10.4) evaluated at the interface.

When writing down the boundary condition for the pressure jump Δp at the interface (corresponding to (9.4)), one has to take into account the specific geometry of a Hele-Shaw cell. This expression contains three terms: i) There is a relatively large pressure jump due to the parabolic profile mentioned above. The associated surface curvature is typically about $2/b$. This curvature measured in a direction perpendicular to the plates is approximately independent of the actual position of the interface and it does

not have a relevant effect on the motion. ii) The contribution of the surface curvature κ observed in the $x-y$ plane is proportional to the surface tension γ and to κ. Finally, iii) due to the wetting of the cell's walls by the displaced fluid, Δp is increased by a term proportional to $v_n^{2/3}$ (Park and Homsy 1985). Thus, for viscous fingering (9.4) has the form

$$\Delta p \simeq \frac{2\gamma}{b} + \gamma\kappa + \frac{3.8\ (\mu v_n)^{2/3}\gamma^{1/3}}{b}. \tag{10.5}$$

In a longitudinal cell of width w (Fig. 10.1) there is a single dimensionless quantity which can be used as a control parameter of the problem. In such a system

$$d_0 = \frac{b^2}{w^2}\frac{\gamma}{\mu V} \tag{10.6}$$

is an analogue of the capillary number in (9.4). Here V is the velocity of the injected fluid far from the interface. The experiments to be discussed below have demonstrated that on increasing d_0 from a small (or negative) value various regimes take place concerning both the dynamics and geometry of viscous fingering.

The traditional experiment is carried out using two inmiscible, Newtonian fluids with a *high viscosity ratio*. For example, air can be used to displace glycerine or oil. Injecting an inviscid fluid into a longitudinal Hele-Shaw cell containing a viscous one results in an initial transient behaviour followed by the development of a single finger which propagates along the channel in a stationary way. According to the related experiments (Saffman and Taylor 1958, Tabeling and Libchaber 1986), numerical simulations (Gregoria and Schwartz, Sarkar and Jasnow 1987) and theoretical approaches (Bensimon *et al* 1986), the width of the finger λ for intermediate values of d_0 is close to $w/2$, where w is the width of the cell. In fact, theory predicts $\lambda = w/2$ in the $d_0 \to 0$ limit, while finger widths somewhat smaller than $w/2$ can be observed experimentally and in numerical solutions of the corresponding equations. For large V the single finger shows rather unstable behaviour (see Fig. 9.4).

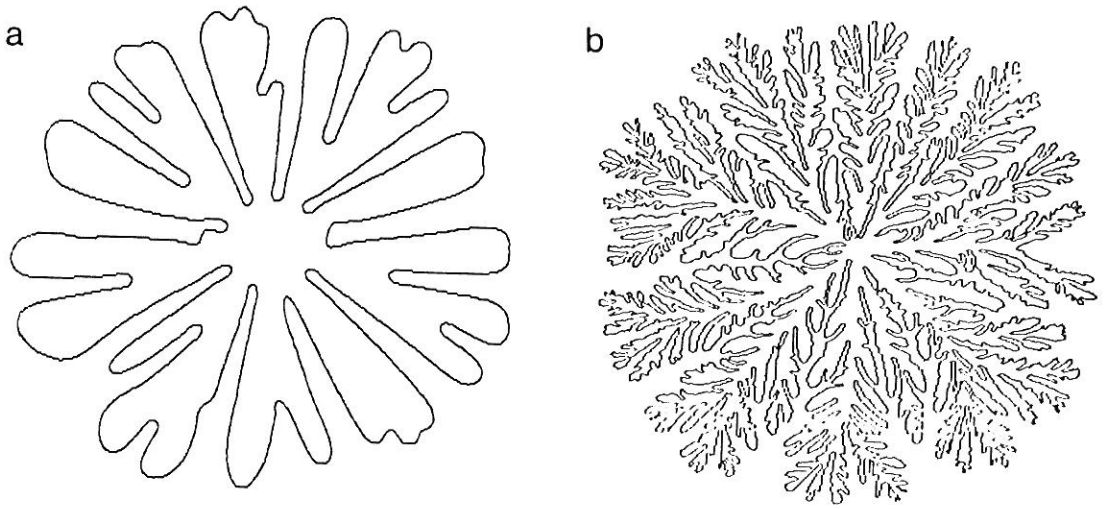

Figure 10.2. Typical viscous fingering patterns obtained in the radial Hele-Shaw cell with glycerine for (a) intermediate and (b) large pressure of the injected air.

In the *radial* Hele-Shaw cell (Paterson 1981, 1985) the stabilizing effect of the side walls is absent and *no steady-state fingers* can develop in the cell. Consequently, the Mullins-Sekerka instability (Saffman and Taylor 1958, Mullins and Sekerka 1963) leads to the growth of disordered interfaces shown in Fig. 10.2. Interestingly, the question whether such viscous fingering patterns become fractals in the large size limit has not been satisfactorily answered yet. For intermediate injection rates (Fig. 10.2a) relatively simple structures can be obtained with an effective radius of gyration exponent corresponding to a fractal dimension close to 1.8 (Rausseo *et al* 1987).

When *large injection rates* are applied (Fig. 10.2b) the growing interface seems to branch randomly without forming holes of increasing size, and the structure can be regarded as *homogeneous* (non-fractal) on a length scale comparable to its diameter. In this case the surface has a geometry analogous to the Peano curve discussed in Section 2.3.1. Similar interfacial patterns have been observed in other types of experiments as well, thus it is useful to introduce a common name for these homogeneous structures. An interface has *dense radial structure* (DRS) if it i) grows outward from a centre, ii) is not a fractal, and iii) has a well defined spherical (circular) envelope.

10.1.2. Fractal viscous fingering

Fig. 10.2 demonstrates that fractal viscous fingering patterns are not expected to grow in the traditional Hele-Shaw cell. However, the situation is completely changed if one introduces some kind of randomness into the experiment by placing a porous medium between the two plates. The investigation of viscous fingering in a random environment can be accomplished by using such model media as layers of small spheres (Maloy *et al* 1985) or carefully manufactured networks of channels having stochastically varying diameters (Chen and Wilkinson 1985, Lenormand and Zarcone 1985, Lenormand 1986).

For a given *random medium* very different regimes of fractal growth can be observed as a function of the applied flow rate or the wetting properties of the injected fluid. The following micromodel (e.g. Lenormand 1986) has been successfully used to investigate various crossovers in the shape of the interface between two fluids moving in a network. The main part of the model is a transparent resin plate consisting of channels and pores cast on a photographically etched mould. The flow is restricted to the channels by appropriately closing the resin plate. In a typical experiment the depth of the channels following the bonds of a square lattice is about 1mm, while their width varies around an average value according to a given distribution. The less viscous fluid is injected into the cell through a hole at the centre of the upper plate.

The two basic geometries are presented in Fig. 10.3 for the case of air displacing very viscous oil wetting the walls of the model. If the injection rate is extremely slow (many hours per experiment), the capillary forces dominate the motion of the interface. These forces may prevent the air from entering very narrow channels, while the interface advances faster at places where the channels have large cross-sections. In this limit the viscous forces and the effects of pressure distribution can be neglected. The above conditions correspond to the *invasion percolation* model with trapping (Section 5.2.), and accordingly, the shape of the region filled with air is reminescent of percolation clusters (the perimeter of a large percolation cluster is shown in Fig. 5.10). The analogy is supported by an agreement between the fractal dimension $D \simeq 1.82$ calculated for invasion percolation with trapping and

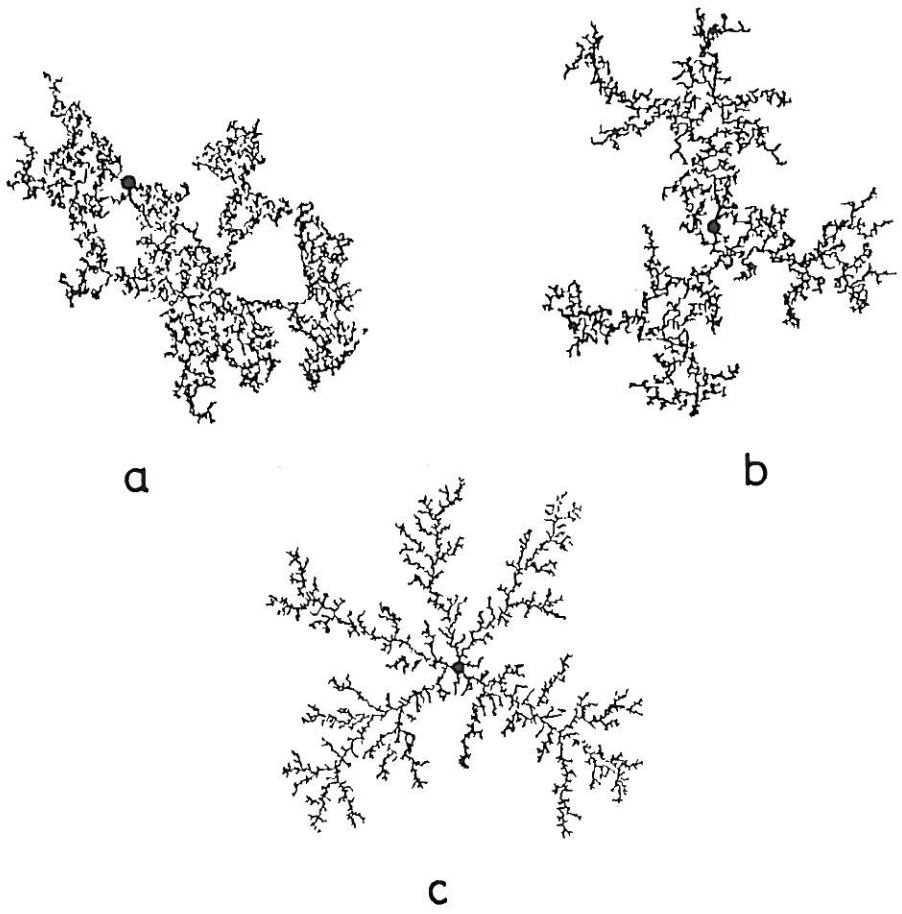

Figure 10.3. The black structures correspond to the channels in which the injected air displaced oil in a radial micromodel consisting of 250,000 capillary tubes having randomly distributed radii. (a) Very slow injection rate: invasion percolation regime, (b) crossover, and (c) high injection rate: in this regime the pattern is similar to DLA clusters (Lenormand 1986).

the value $1.80 < D < 1.83$ determined experimentally.

If the flow rate is considerably increased (few seconds per experiment) the capillary forces become negligible compared with the viscous ones. In this case, it is the non-local distribution of pressure within the more viscous fluid which dominates the flow. The situation is very similar to that existing in an ordinary Hele-Shaw cell, except that the varying channel widths represent local fluctuations in the parameter d_0. As a result fractal viscous fingering patterns are observed (Fig. 10.3c) having a geometry almost in-

distinguishable from diffusion-limited aggregates (Chen and Wilkinson 1985, Lenormand 1986). Decreasing the level of randomness in the channel widths leads to structures analogous to noise-reduced DLA clusters (Kertész and Vicsek 1986).

Porous media can also be modelled by placing a layer of randomly distributed glass spheres of diameter about 1mm between the plates of a Hele-Shaw cell (Maloy *et al* 1985). In these experiments DLA type patterns have been observed as well. The corresponding fractal dimension can be calculated by digitizing the pictures taken from the growing structure. The application of methods described in Section 4.2. gives an estimate $D \simeq 1.62$ somewhat lower than $D \simeq 1.71$ characteristic for two-dimensional DLA clusters. In such experiments the width of an individual finger is comparable to the holes between the glass spheres. If the injected fluid preferentially wets the medium, the structure of the interface remains qualitatively the same, but the finger width becomes much larger than the pore size (Stokes *et al* 1986).

Cells packed with non-consolidated, crushed glass have also been used to study viscous fingering in three dimensions (Clèment *et al* 1985) which represents a more important case from the practical point of view. The observed interfaces are complex, however, it is quite difficult to obtain an accurate estimate for the fractal dimension from the experimental data. An elegant three-dimensional experiment related to viscous fingering will be discussed in Section 10.4.

One interesting aspect of the micromodels is related to a special distribution of channel widths. Assuming that a fraction of the channels is completely blocked, while the rest of them have the same width, one arrives at networks of channels corresponding to *percolation* clusters (Oxaal *et al* 1987). Let us assume that the concentration of conducting channels is equal to p. Then at the percolation threshold, p_c, there exists a fractal network of open channels in the system and the model can be used to investigate the phenomenon of viscous fingering on a fractal. The incompressibility of the trapped fluid regions and the presence of singly connected paths gives rise to a number of non-trivial effects in such experimental systems. Most importantly, the fractal dimension of the viscous fingering patterns is considerably

reduced compared with its value on networks, where each of the channels has a finite conductivity of varying degree. Since a finger which connects two sites on the backbone must pass through all the singly connected bonds on the link between these two sites, the overlap of patterns obtained for independent injections is relatively high. The resulting fractal dimension is $D \simeq 1.3$.

Fractal viscous fingering can be observed in systems *without any randomness imposed* by stochastic boundary conditions. Using a *smectic A liquid crystal* as the more viscous fluid in a radial Hele-Shaw cell it is possible to study a fractal $\rightarrow$ non-fractal crossover in the morphology of viscous fingers as the role of the inherent fluctuations decreases (Horváth *et al* 1987). Fig. 10.4 shows the patterns which are obtained if gaseous nitrogen of varying pressure is injected into an 8CB Licrystal (BHD) at a temperature of 24°C corresponding to the smectic phase. The experiments with liquid crystals are usually carried out in a cell which is smaller than the standard versions. The linear size w is typically in the region of 7-10 cm, while the distance between the plates is about $b \simeq 40\mu$m.

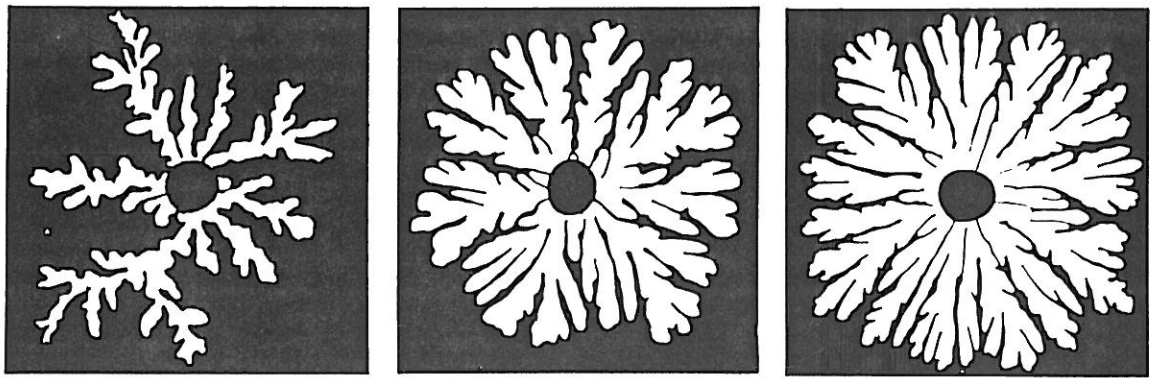

Figure 10.4. Increasing the pressure of air injected into a layer of smectic A liquid crystal results in a crossover in the global behaviour of the patterns. (a) For low pressures ($p = 30$mmHg) the interface has a structure analogous to that of DLA clusters, while (c) the patterns become homogeneous (non-fractal) for large pressures ($p = 70$mmHg) (Horváth *et al* 1987).

If the applied pressure is small, randomly branching interfacial pat-

terns are observed whose open structure is similar to that of DLA clusters. The fractal dimension associated with the bubble shown in Fig. 10.4a is close to 1.6. However, this open geometry crosses over into a homogeneous DRS (Fig. 10.4c) when the pressure of the injected N_2 is increased.

The above results can be interpreted on the basis of the specific internal structure of smectics. If the plates are not prepared to provide an ordering of the molecules on a length scale comparable to w, the director (the local orientation of the elongated liquid crystal molecules) s randomly changes within the sample. As a result of the *orientational disorder* the screening effects become dominant. The mechanism for the relevance of fluctuations is provided by the fact that the shear viscosity in an anisotropic liquid is strongly orientation dependent, thus the local ordering of the molecules indicates "easy" or "hard" local flow directions. The application of large pressures is likely to destroy the state in which a well defined director can be associated with the different parts of the sample. In this case the behaviour is expected to be analogous to that observed for isotropic fluids. Indeed, Fig. 10.2b and Fig. 10.4c are in qualitative agreement.

In addition to the above discussed examples, the structure of viscous fingering patterns has fractal properties (Fig. 1.e) analogous to DLA if two miscible, non-Newtonian (or shear-thinning) fluids are used in the experiments (Nittmann *et al* 1985, Daccord *et al* 1986). In such a system the surface tension is practically zero and the flow velocity is determined by the expression

$$\vec{v} \sim (\nabla p)^k, \tag{10.7}$$

where the exponent k is in a typical experiment, larger than 1. For Newtonian fluids $k = 1$ (10.4). Correspondingly, the pressure distribution satisfies the equation $\nabla(|\nabla p|^{k-1}\nabla p) = 0$, which is also different from the Laplace equation (9.1). Because of the $(\nabla p)^k$ term in (10.7), for $k > 1$ the preferential growth of the tips is more pronounced in the non-Newtonian case than for Newtonian growth.

The related experiment can be carried out by injecting dyed water into

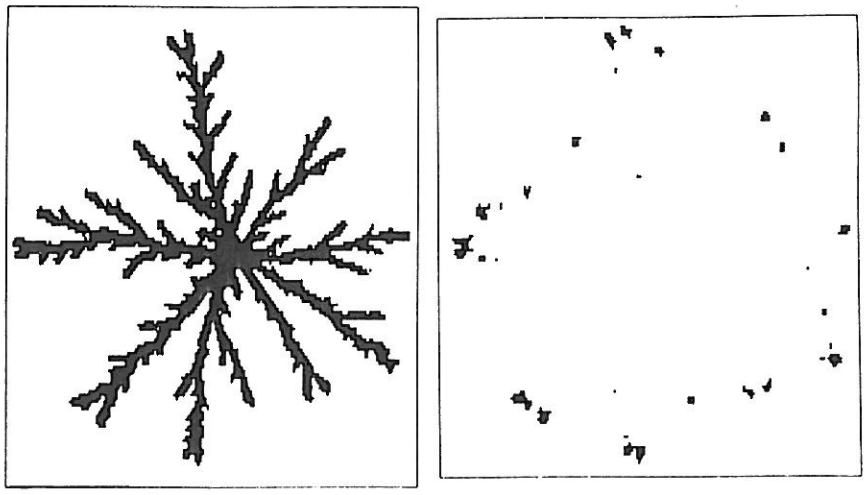

Figure 10.5. (a) Digitized image of a fractal viscous fingering pattern obtained by injecting water into a non-Newtonian, miscible liquid. (b) The region of fastest growth is visualized by subtracting the images of the same finger photographed at slightly different times (Daccord *et al* 1986).

a layer of aqueous solution of polysaccharide. The viscosity of the polymer solution depends on the actual velocity, but it is usually $10^2 - 10^4$ times larger than that of the pure water. Fig. 10.5 shows the digitized image of a representative pattern together with a picture demonstrating the preferential growth of tips. The measured fractal dimension $D \simeq 1.7$ is close to the DLA value in this case as well. Analogous patterns are grown if water is injected into clay slurry (Damme *et al* 1986), which is a system of practical importance.

Fig. 10.5 also indicates a possible method to calculate the *multifractal spectra* describing the distribution of experimental growth velocities (Nittmann *et al* 1987). These velocities can be estimated by simply subtracting subsequent images of the same finger taken at slightly different times. Then an analysis along the lines discussed in Section 3.2 and Section 9.4. can be applied to determine the spectrum of fractal dimensions $f(\alpha)$. Because of the limited available resolution it is not possible to obtain quantitatively accurate results using this technique; however, the qualitative behaviour of the calculated quantities has been found to be of DLA type.

10.1.3. Viscous fingering with anisotropy

The crucial role of the anisotropy of surface tension in the formation of interfacial patterns has recently been demonstrated by a number of theoretical approaches and computer simulations (Sections 9.2.2. and 9.3.). These studies have also indicated that diverse sources of anisotropy may lead to similar results. Experiments on viscous fingering in appropriately modified versions of the radial Hele-Shaw cell represent a valuable tool for the investigation of the combined effects of anisotropy and the driving force (pressure difference) in real systems. In particular, the conditions leading to the stabilization or destabilization of the tips of fingers are of special interest.

Anisotropy can be introduced into the experiments on viscous fingering in isotropic liquids by *engraving a mesh* on the surface of the glass plates of the cell (Ben-Jacob *et al* 1985). For a given set of grooves there are two parameters which can be monitored in the course of an experiment. Increasing the distance b between the two plates generally corresponds to decreasing the effective anisotropy, while in order to investigate the role of driving force one changes the pressure of the less viscous fluid. In the basic version of such experiments air is injected into an ordinary viscous liquid (e.g. glycerine). The grooves commonly have a depth, a width and an edge-to-edge distance about 0.5-1.0 mm. It has been demonstrated that a small separate bubble located at and moving together with the tip of a growing finger introduces an effective anisotropy as well (Couder *et al* 1986a, 1986b) leading to interfaces analogous to one of the structures shown in Fig. 9.3 (middle picture of Ib).

The types of patterns which are observed if the grooves are engraved according to the geometry of a triangular lattice are shown in Fig. 10.6. In this set of experiments b is fixed and the *morphological changes* are obtained as a function of the increasing pressure p. For low values of p faceted growth (a) is found. When increasing the pressure the interface becomes unstable against tip splitting (b), and an entirely disordered structure develops in the cell. A needle crystal type pattern having stable tips and a sixfold symmetry (c) is observed, if p is further increased. Finally, for the largest pressures applied, the radius of curvature of the tips is reduced and side branches appear

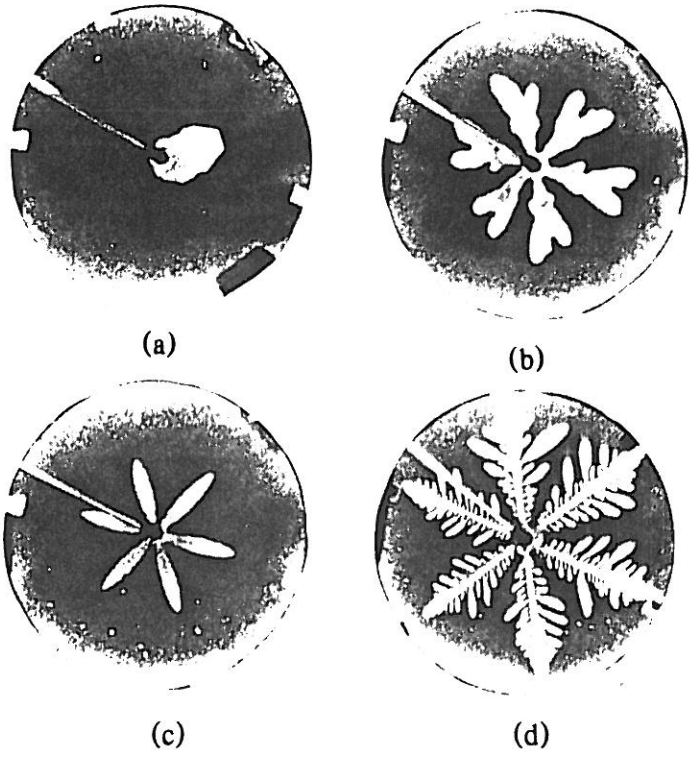

Figure 10.6. These patterns are observed in a radial Hele-Shaw cell as a function of increasing pressure if one of the plates has a triangular lattice engraved on it.

on the main dendrites (d). The sixfold symmetry due to the underlying mesh is approximately conserved in this case, in analogy with the structure shown in Fig. 9.10. Correspondingly, this pattern is likely to have a non-trivial radius of gyration exponent. However, such measurements have not been carried out.

A rich variety of morphological phases can also be obtained in a simpler system, where a set of parallel grooves is etched on one of the plates (Horvàth *et al* 1987). A systematic series of experiments with this geometry allows the construction of a *morphological phase diagram* of the non-equilibrium patterns observed in the system. The results are summarized in Fig. 10.7, where the phases are indicated by their typical patterns.

This figure demonstrates the complexity of the phenomenon of viscous fingering with anisotropy as a function of the driving force. Depending on the

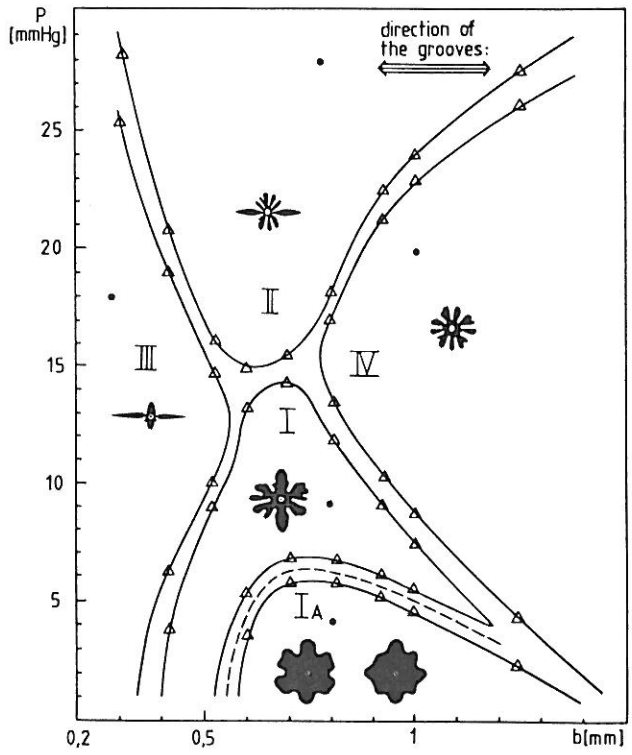

Figure 10.7. Morphological phase diagram of the interfacial patterns obtained in the radial Hele-Shaw cell with a uniaxially engraved plate. Varying the pressure (p) and the distance of the plates (b) relatively sharp transitions can be observed between the different phases denoted by characteristic patterns (Horváth *et al* 1987).

value of the parameters b and p, the direction of the stable growth changes and virtually all of the possible geometries can be achieved. The *crossover* from one kind of pattern to another one is quite *sharp* taking place in a narrow pressure interval. For low pressures the growth can be stable in the "hard" direction (perpendicular to the grooves) and unstable (splitting tips) along the grooves. This situation is reversed as the pressure is increased. Another typical case is when stable tips grow in both directions.

The experiments with an imposed anisotropy suggest the following picture of the interplay of anisotropy and pressure difference. It is plausible to assume that the mechanism by which a tip growing in the direction perpendicular to the grooves is coupled to the channels is different from that dominating in the case of parallel growth. The response of these mecha-

nisms to the changes in the pressure is expected to be different; the effective anisotropy in the perpendicular direction decreases, while in the parallel direction it increases as larger pressures are applied.

The presence of the direction dependent couplings explains the non-trivial behaviour of the effective anisotropy as a function of b and p and this is the reason leading to the complex phase diagrams of the type shown in Fig. 10.7. It is important to point out that the above situation is typical, because in the real systems exhibiting pattern formation the anisotropy has several sources. In fact, this can be taken into account by the two terms in the boundary condition (9.4), where the equilibrium and kinetic contributions are represented separately. For fast growth the anisotropy in the kinetic coefficient β dominates the growth, but in the slow regime it is not expected to play an important role. If the angular dependence of the static surface tension γ is different from that of β, the *competition* between the anisotropies gives rise to a rich behaviour.

In the experiments discussed above the anisotropy was imposed externally by engraving a macroscopic grid on the plates. Another alternative is to use a liquid which is *inherently anisotropic on a microscopic scale* (Buka *et al* 1986). This can be achieved by placing a liquid crystal having an angular dependent shear viscosity into the cell. The anisotropic nature of liquid crystals is manifested only if there exists a well defined local director, i.e., the elongated molecules are directed approximately uniformly in the given region. In the experiments with *nematic liquid crystals* the flow of the liquid itself provides the necessary orientation. As soon as the fluid pushed by the injected air starts flowing away from the central hole, the molecules become radially oriented (this can be checked by crossed polarizers). Nevertheless, for low injection rates the growing interface goes through repeated tip splittings and one obtains a pattern characteristic for Hele-Shaw cells with isotropic liquids (see Fig. 10.2a).

However, increasing the flow rate results in the qualitatively different behaviour shown in Fig. 10.8. The tips become stable and the observed structure looks like a snowflake type dendritic crystal. A further increase of the pressure induces another morphological transition: the tip splitting

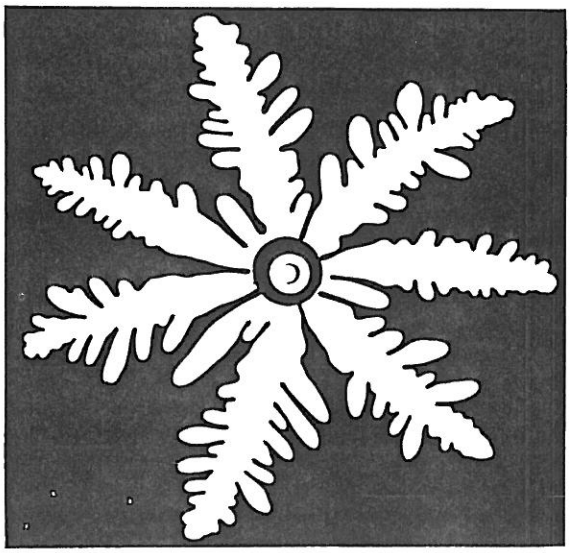

Figure 10.8. Viscous fingering pattern obtained by injecting air into a thin layer of a nematic liquid crystal (7A Licrystal, BDH) at room temperature. The radial alignment of the molecules and the anisotropic shear viscosity results in stabilization of the tips (Buka *et al* 1986).

mechanism is restored and the resulting patterns (Fig.10.1d) seem to be space filling (in analogy with Fig.10.2b). The above described tip splitting → dendrites → tip splitting *reentrant transition* can be observed as a function of the decreasing temperature as well (Buka *et al* 1987). A possible qualitative interpretation of the above transitions is based on the assumption that for slow flow the molecules are not orientated enough to produce the necessary anisotropy to stabilize the tips. On the other hand, for large pressures the director at the interface is likely to become turbulent and the local ordering of the molecules is lost.

Carrying out experiments with a smectic A liquid crystal can be used to demonstrate the effects of *inherent uniaxial anisotropy* (Horváth *et al* 1987). The local director in smectics is not dependent on the applied pressure as much as in the case of nematics, therefore, it is possible to investigate the influence of a preliminary allignment of the molecules. During such experiments the temperature of the sample is increased to a value corresponding to the isotropic phase and then an external magnetic field parallel to the plates

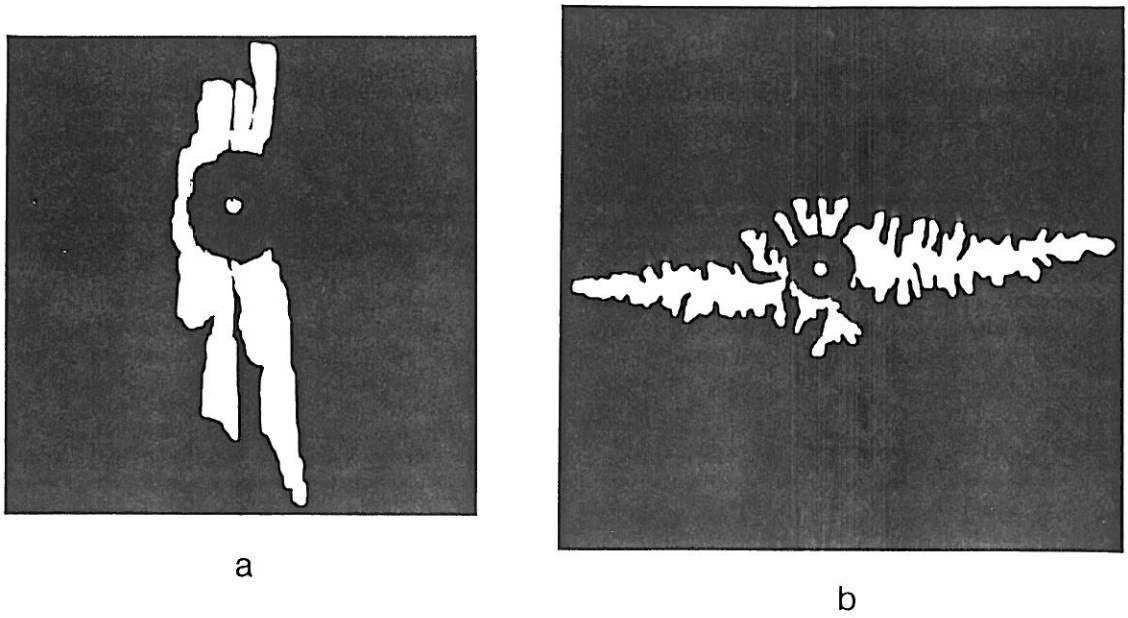

Figure 10.9. If the molecules of the smectic liquid crystal are preoriented by an external magnetic field, the interface becomes elongated. (a) For small pressure the pattern is elongated in a direction perpendicular to the field; (b) at $p \simeq 35$mmHg a crossover takes place and the fingers grow easier parallel to the field (Horváth *et al* 1987).

is applied. The field aligns the molecules along its direction and as the liquid crystal is cooling down this orientation freezes in. For a given pressure of the injected air the overall shape of the bubbles changes from nearly circular to an elongated one as the magnitude of the magnetic field is increased.

In the case of preoriented samples the following crossover can be observed. For very low injection rates the interface is elongated in a direction perpendicular to the director (Fig. 10.9a). This is understandable, since in smectic A liquid crystals the molecules are ordered into separate layers perpendicular to the director and these layers can slip on each other relatively easily. However, when the pressure is increased, the structure of the patterns changes qualitatively. It becomes more ramified and elongated parallel to the field (Fig. 10.9b) resembling DLA clusters obtained by using an anisotropic sticking probability (Fig. 6.7). A possible explanation for this behaviour is that the larger pressure gradient generates dislocations of the layers and these dislocations move easier in a direction parallel to the field

(perpendicular to the layers).

10.2. CRYSTALLIZATION

Non-equilibrium solidification processes are known to lead to complex geometrical patterns. There are two basic types of dendritic crystallization: i) in a pure undercooled liquid and, ii) in an isothermal liquid mixture. Here we used the term crystallization (instead of solidification) to express the fact that crystals can grow in heat treated amorphous (i.e. already solid) materials as well. In the undercooled case it is the distribution of temperature which represents the rate limiting quantity, while during isothermal crytallization the concentration of the diffusing atoms dominates the phenomenon. In the following the term diffusion will be used for the transport of both heat and mass.

The equations describing crystallization (Langer 1980) in the limit of large diffusion length, $l = 2C/v_n$, and large diffusivity in the crystalline phase are the same as (9.1-9.4), where C is the diffusion constant and v_n is the normal velocity of the interface. In many cases these assumptions are not valid, and instead of (9.1) it is more appropriate to describe the process by the *diffusion equation* expressing the conservation of heat or mass

$$C_i \nabla^2 u = \partial u / \partial t, \tag{10.8}$$

where u denotes either temperature or $\tilde{\mu}$, and C_i is the diffusion constant in substance i. Here $\tilde{\mu}$ is the difference between the chemical potential μ and its equilibrium value for two phase coexistence at the temperature at which the crystallization takes place. If the diffusivity in the crystallized phase is not much larger than in the surrounding one, the boundary condition (representing a continuity equation at the surface) (9.2) should be modified to have the form

$$v_n = [c_{cryst}(\nabla u)_{cryst} - c_{surr}(\nabla u)_{surr}]\hat{\mathrm{n}}, \tag{10.9}$$

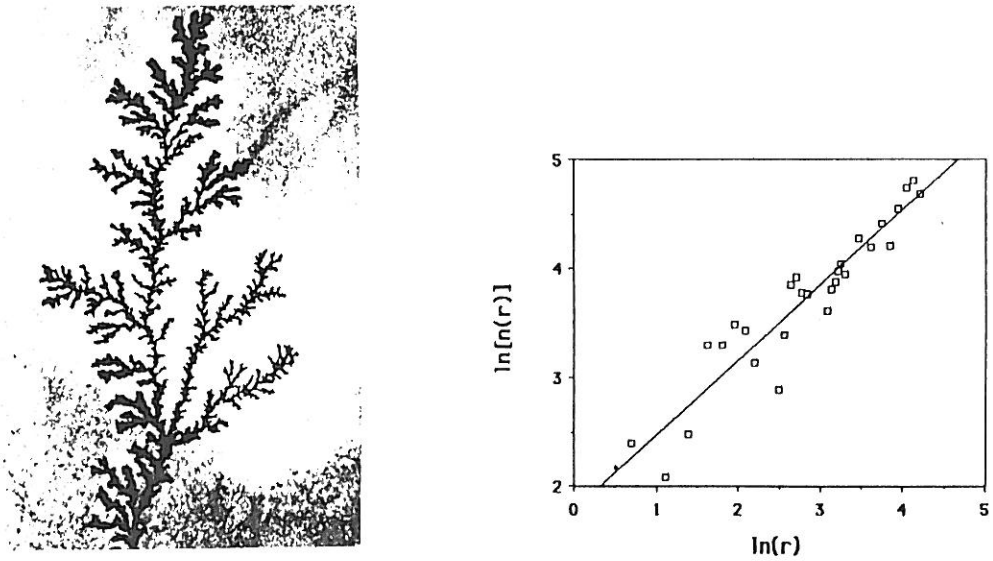

Figure 10.10. Part of the tree-like crystalline phase growing in an amorphous $GeSe_2$ thin film heat treated at 220°C (left). The plot on the right gives an estimate $D \simeq 1.69$ for the fractal dimension of the pattern shown in part (a) (Radnóczy *et al* 1987).

where the subscripts indicate quantities in the crystalline and the surrounding phases (the latter can be either liquid or amorphous). It is important to be aware of the fact that unlike viscous fingering the approximations leading to the set of equations (9.1-9.4) are frequently not satisfied for crystallization. In some cases this is the reason why the observed complex patterns are not fractals.

Because of the regular microscopic structure of the growing phase, the development of single crystals is typically dominated by the anisotropy of the surface tension. Accordingly, the patterns observed in these experiments are more or less symmetric. To obtain randomly branching fractal structures one can study crystallization in an *amorphous thin film* (Radnóczy *et al* 1987). In this system, the effects caused by the anisotropic surface tension are expected to be small because the new phase is polycrystalline with preferred growth directions randomly distributed.

Fig. 10.10a shows a highly ramified polycrystalline branch grown in an amorphous $GeSe_2$ thin film. Such pictures can be obtained by heat treating

the amorphous sample prepared by vacuum evaporation and taking transmission electron micrographs of the patterns. Crystallization is observed at 220°C, which is well below the $GeSe_2$ glass transition temperature of 265°C. Digitizing the image an estimate for the fractal dimension of the pattern shown in Fig. 10.10a can be given. One counts the number of dark pixels $n(r)$ at a radius r from the centre of mass and assumes the scaling $n(r) \sim r^{D-1}$. From the related log-log plot shown in Fig. 10.10b the value $D \simeq 1.69$ is obtained (Radnóczy et al 1987) which is very close to the fractal dimension of diffusion-limited aggregates generated in two dimensions.

Fractal crystallization in the present example is likely to be due the mechanism analogous to that occurring in the isothermal solidification of a liquid mixture. This mechanism represents one of the ways how the Mullins-Sekerka instability is manifested (Section 9.1.). Let us assume that the main components are not present with their exact stoichiometric concentrations, e.g., $c_{Se} > c_{Ge}/2$. Then, if the temperature is higher than the amorphous-solid transition temperature, crystallization of $GeSe_2$ starts at places which are somewhat warmer or contain more nucleation centres. The crystallizing phase expels excess Se so that the amorphous region becomes further enriched in Se. This excess of Se must diffuse away before further crystallization can occur. Concentration gradients are greatest at the most advanced parts of the interface, and the corresponding instability drives the system.

To understand the phenomenon better, a few further remarks are in order. An estimation for the velocity of the interface and for the diffusion constant of Se in $GeSe_2$ at 220°C suggests that the diffusion length l in the bulk is very small compared with the size of the pattern. Thus, a fractal interface can not be formed through bulk diffusion of atoms. However, surface diffusion coefficients are commonly measured to be 10^8-10^{10} times larger than those of the bulk. Advancement of the crystallization front through *surface diffusion* would account for the scale invariance of the observed structures. In a solid-solid phase transition a number of additional factors are expected to affect the results. The specific volume of the crystalline phase is smaller than that of the amorphous state and because of this, long-range elastic forces are created during the growth which may also play an important role

in the fractal growth.

Interestingly, a qualitatively different behaviour can be observed in a closely related system of vacuum deposited $Al_{0.4}Ge_{0.6}$ amorphous thin films (Ben-Jacob *et al* 1986). After heat treating the sample at a temperature of 230°C *dense radial structures* (DRS) have been found to grow at many sites (Fig. 1a). As revealed by electron diffraction studies the growing phase is polycrystalline Ge, which is surrounded by an Al-rich region being a nearly perfect crystal. One of the possible reasons for the apparent non-fractality of the obtained patterns may be the relative shortness of the diffusion length. The physics of dense radial growth is not completely understood yet and it has recently been subject to intensive theoretical and experimental investigations (Grier *et al* 1987, Alexander *et al* 1988, Goldenfeld 1988).

A number of further experiments on pattern formation in thin films have demonstrated the development of complex interfacial structures. Random dendritic structures were observed to grow in $NbGe_2$ sputter deposited onto silica (Elam *et al* 1985). The skeleton of these objects was found to have a fractal dimension close to 1.7. In some of the cases the obtained structures have been suggested to be fractals, however, in the light of recent results on dense radial growth it is more plausible to assume that the geometry of the observed patterns is analogous to the dense radial structure. The complex crystalline phosphorlipid domains growing in monomolecular layers (Miller *et al* 1986) and the patterns observed in ion irradiated Ni-Mo alloy films (Liu *et al* 1987) seem to fall into this category (schematically shown in Fig. 9.3, IIa). Note, that one can call a physical object fractal if the corresponding non-integer scaling is well satisfied at least for two orders of magnitude (Section 2.1.). (Sometimes one makes exceptions when the scaling holds with particularly good accuracy.)

Randomly branching, fractal dendritic growth of single crystals can be produced by *introducing fluctuations externally* (Honjo *et al* 1986). Consider a supersaturated solution of NH_4Cl between two smooth parallel plates separated by a small distance of $\sim 5\mu$m. In this system the anisotropy of the surface tension causes very regular dendritic growth. Strong random perturbations can be imposed by replacing one of the plates with another

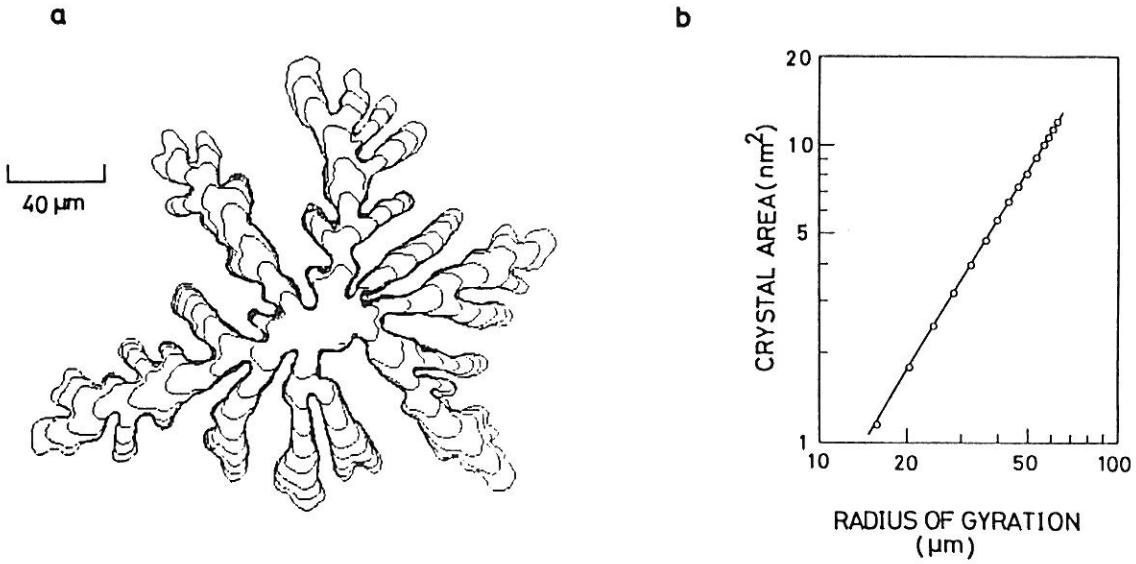

Figure 10.11. (a) Superimposed picture of a growing NH_4Cl crystal taken at 20-sec intervals. The growth is confined between glass plates separated by 5μm. (b) Estimating the fractal dimension of the pattern (a) from the dependence of the crystal's area on its radius of gyration ($D \simeq 1.67$) (Honjo *et al* 1986).

one having a *rough surface.* This experiment is related to those designed to study viscous fingering in random media. On the other hand, it represents an opposite approach to engraving on the surface of the Hele-Shaw cell a regular lattice (Section 10.1.2 and 10.1.3.). There, anisotropy had to be introduced because the fluid had an isotropic surface tension, while in the present case one intends to get rid of the anisotropy by scratching the plate. It should be noted that for very large undercoolings some of the dendrites can grow in a direction different from the crystallographic one even in a cell without randomness. In such cases spontaneous splittings of the tips have been found.

Fig. 10.11a shows a typical pattern obtained with a plate having a characteristic length of roughness approximately equal to 7.5 μm. The development of the structure is indicated by superposing the digitized pictures corresponding to subsequent stages of the process. As in DLA, those are only the tips which advance significantly. The width of the fingers is roughly the same as the mean length of the roughness. The interface is very similar to the small scale viscous fingering patterns observed in Hele-Shaw cells with

randomness, and is also reminiscent of the computer simulation shown in Fig. 9.13. The dependence of the crystal's area on the radius of gyration is displayed in Fig. 10.11b. Although fractal scaling with an exponent $D \simeq 1.67$ is found on a length scale somewhat less than a decade, the data points follow a straight line with a surprising accuracy. This suggests the continuation of similar behaviour to considerably larger sizes.

The overlapping patterns shown in Fig. 10.11a provide a suitable basis for the *multifractal analysis* of the growth velocities (Ohta and Honjo 1988). Let us define the growth probability distribution as a set of normalized velocities $p_j = v_j / \sum_j v_j$, where v_j is the normal velocity of the interface at the jth pixel point. Then the $f(\alpha)$ spectrum can be determined using the method discussed in Chapter 3., Section 6.1.4. and at the end of Section 9.4.

There are several ways to determine the set of v_j-s. One possibility is to calculate the velocity of the interface directly by measuring the length of the interval which is perpendicular to the surface and is bounded by two successive perimeter positions. The boundary condition (9.2) can be used for an indirect determination of the interfacial velocity through the knowledge of the temperature gradients at the surface. These gradients are calculated by numerically solving the Laplace equation. This is the same procedure which was used to study the multifractal properties of the growth site distribution of off-lattice diffusion-limited aggregates.

The results for $n(p)$ and $f(\alpha)$ are displayed in Fig. 10.12, where $n(p)dp$ is the number of places with a growth probability between p and $p + dp$. Fig.10.12a demonstrates that the direct determination of the growth velocities is rather limited by the resolution. Thus, this method does not allow the calculation of $f(\alpha)$ for $\alpha > 1$, because this is the region in which low growth probabilities give the dominant contribution. The $f(\alpha)$ spectrum determined from the calculated gradients is in good agreement with the related results obtained for DLA clusters. The limiting cases $D_0 \simeq 1.63$, $D_1 \simeq 1.13$, $\alpha_{-\infty} \simeq 9.4$ and $\alpha_{\infty} \simeq 0.6$ are in reasonable accord with the corresponding numerical and the following theoretical results for DLA: $D_0 = 5/3$, $D_1 = 1$ and $\alpha_{\infty} = 2/3$.

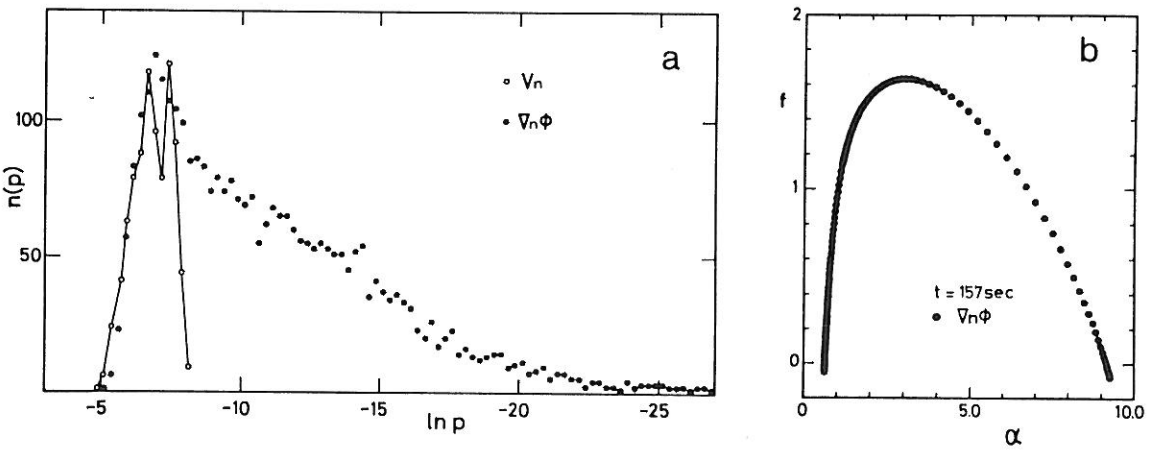

Figure 10.12. (a) The distribution functions, $n(p)$, obtained from determining the velocity of the interface of the experimental pattern shown in Fig. 10.11a. The velocities were both measured directly (V_n) and calculated from the corresponding temperature gradients ($\nabla_n \phi$). (b) The spectrum of fractal dimensionalities ($f(\alpha)$) determined from the calculated data for the temperature gradients (Ohta and Honjo 1988).

10.3. ELECTROCHEMICAL DEPOSITION

In a typical experiment on electrodeposition two elecrodes are immersed into an ionic solution and one observes the structure made of metal atoms deposited onto the cathode. The anode and the cations are of the same metal and a stationary concentration of the cations is maintained by the dissolution of the anode itself. The most common experimental setup (Matsushita *et al* 1984) is similar to that of the radial Hele-Shaw cell: the electrolite is kept between two close glass plates with a circular anode surrounding the cathode located at the centre. The typical sizes are 10 cm (diameter) and 0.5 mm (distance of the plates), while the applied voltage is in the range of 1 to 20 Volts.

The growth of electrodeposits involves a number of simultaneous processes which lead to a quite complicated behaviour of the system as a function of the applied voltage and chemical concentration. As a result, the experi-

mentally observed *morphological phase diagrams* are rich (Grier *et al* 1986, Sawada *et al* 1986) and do not entirely coincide even for the same values of the above parameters. Deviations from a purely Laplacian growth are expected to occur due to the following problems: i) the transport of the ions is affected by convection of the fluid, ii) at high voltages gas evolution takes place because of electrolysis of water, iii) the ion can be driven both by the concentration gradient and the electric field, and iv) the actual voltage drop within the electrolite is unknown (unless reference electrodes are used), because of the voltage drops within the deposit and in the surface layer of the electrodes.

To see the relation of electrochemical deposition to Laplacian growth one first assumes that the effects of convection can be neglected on a length scale much larger than the distance between the plates. Furthermore, let us suppose that only one kind of the ions (having a local concentration c) is electroactive. The total current of this ion $\vec{\mathrm{j}}$ (due to both diffusion and drift in the field) is proportional to the gradient of the associated electrochemical potential (e.g. Kessler *et al* 1988)

$$\mu = A(T) + kT \ln c + q\phi, \tag{10.10}$$

where $A(T)$ is a temperature dependent constant, k is the Boltzmann factor, q is the electric charge per ion and ϕ is the electric potential. Next we introduce the dimensionless diffusion field $u = \mu/qV$ (with V denoting the applied voltage), and note that in the quasi-stationary limit the divergence of the total current vanishes, i.e., $\nabla\vec{\mathrm{j}} \simeq \nabla^2 u = 0$.

As an extension of the above conservation law to the interface one obtains the boundary condition concerning the velocity of the interface $v_n \sim \hat{\mathrm{n}}\,\vec{\mathrm{j}} \sim \hat{\mathrm{n}}\nabla u$ in accord with (9.2). It is less straightforward to specify the boundary condition prescribing the value of u on the growing interface. It can be shown that in the limit of small growth rate this last boundary condition becomes analogous to (9.4) (without the kinetic term). In general, however, the condition of local thermodynamic equilibrium is not satisfied in electrodeposition processes and the kinetics of charge transfer at the interface

results in a relation for u on the surface more complicated than (9.4). On the other hand, in the far-from-equilibrium limit the interface acts as a perfect absorber and this condition corresponds to the situation characteristic for DLA. It has also been argued that in the case of dense radial growth the potential at the interface is determined by the resistivity of the filaments (in other words by the voltage drop across the deposit).

The above mentioned *complex reaction kinetics* at the interface is likely to be the reason for the *rich behaviour* of electrochemical deposition. In fact, it is only in the process of electrodeposition that the three basic types of patterns (homogeneous, random fractal and dendritic) can be observed without changing the conditions of the experiment qualitatively (Grier *et al* 1986, Sawada *et al* 1986). This is demonstrated by the bottom row of Fig. 1., where zinc metal deposits of various morphologies are displayed. These rather different patterns were obtained as a function of the $ZnSO_4$ concentration and the applied voltage only. For the homogeneous or dense radial structure $D \simeq 2$, while the value $D \simeq 1.65$ obtained for the random fractal patterns (Matsushita *et al* 1984) is in good agreement with the DLA result. Estimates for the fractal dimension of the observed dendritic patterns have not been reported.

The differences in the macroscopic geometrical properties of the observed patterns is in a close relation to their microscopic structure. This can be shown using electron microscopy and x-ray diffraction for examining the deposits. Transmission electron micrographs suggest that during the dendritic and tip splitting modes of growth the structures are different on the microscopic level as well (Grier *et al* 1986). In Fig. 10.13a a small part of a DLA-like, random fractal deposit is displayed. The isotropic rings in the inset (which is a selected area diffraction pattern from such a region) demonstrate that there is no long range ordering of atoms in the tip splitting deposits. On the other hand, micrographs taken from the dendritic tips (Fig. 10.13b) suggest that they are characterized by large, rounded crystal facets. In addition, the corresponding diffraction patterns (inset in Fig. 10.13b) consist of well defined diffraction peaks indicating long range order.

As in the case of diffusion-limited deposition models (Section 6.2.)

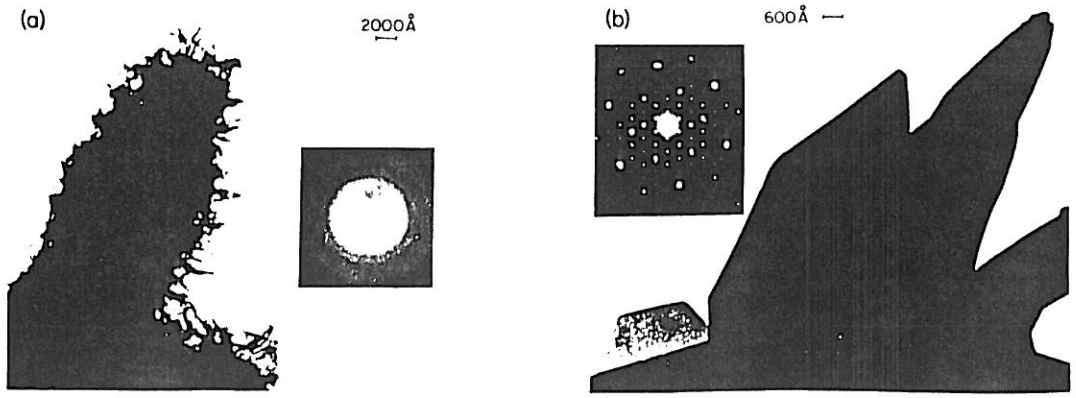

Figure 10.13. Transmission electron micrographs and diffraction patterns of electrodeposited zinc. (a) Picture of a tip observed in the DLA-type regime. The diffuse rings in the diffraction pattern (inset) indicate amorphous microstructure. (b) Dendritic growth with crystalline microstructure (demonstrated by the superlattice diffraction pattern shown in the inset) (Grier *et al* 1986).

studies of electrochemical deposition onto *linear electrodes* provide further information about the growth. In particular, this arrangement is practical for carrying out three-dimensional experiments (Brady and Ball 1984). More importantly, in this approach an ensemble of separate metal trees is found to grow during the process of deposition (Fig. 10.14) (Matsushita *et al* 1986). This feature of the experiment is helpful to strengthen the analogy between DLA and electrodeposition. To describe the distribution of trees in a quantitative manner, the picture of the deposit is digitized, and the size of a given tree is defined as the number of pixels s belonging to it. Then n_s the number of trees of size s is determined making an average over several forests of approximately the same size.

Assuming that for intermediate s the *tree-size distribution* scales as $n_s \sim s^{-\tau}$ the estimate $\tau \simeq 1.54$ can be obtained for the exponent describing the algebraic decay of n_s. This value is in remarkable agreement with the related result for τ determined from large scale simulations of diffusion-limited deposition (see the end of Section 6.3.).

Electrochemical *polymerization* of conducting polypyrrole has also

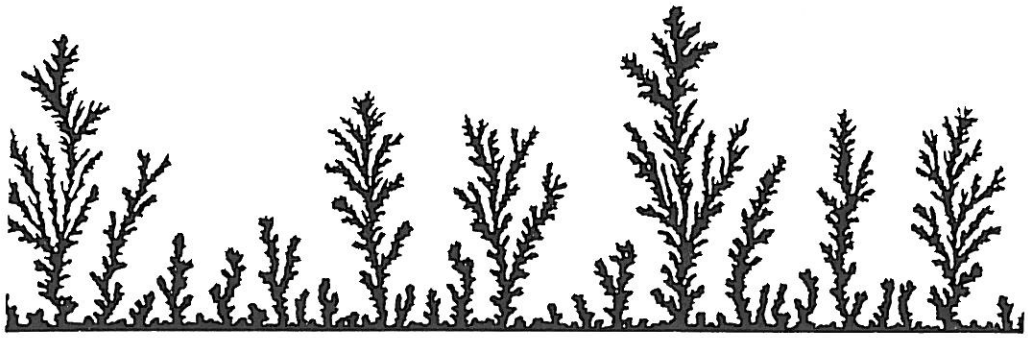

Figure 10.14. Representative picture of a forest of zinc metal trees deposited along a linear carbon cathode. The actual size of this part of the sample is about 6cm (Matsushita *et al* 1985).

been shown to exhibit rich behaviour (Kaufmann *et al* 1987). An important difference between these experiments and electrochemical deposition of metal ions is that the polypyrrol monomer is a neutral species. Polypyrrol is grown by the removal of two electrons from pyrrole monomers and the subsequent polymerization with loss of alpha hydrogens. In addition, the pyrrole chains are oxidized with about one hole, and one counterion, for every three monomer units. Because of the neutrality of the pyrrol monomers the experiment is subject to a smaller number of side effects of electrical origin than the electrodeposition of metal ions. This could be the reason for the observation that in the polymerization experiment an increase of the voltage produces a dendritic $\rightarrow$ tip splitting crossover, while in the case of depositing ions, increasing V results in a tip splitting $\rightarrow$ dendritic morphological transition.

10.4. OTHER RELATED EXPERIMENTS

In this Section two more examples for Laplacian growth will be described. i) Dielectric breakdown represents a typical random growth process. It occurs whenever the electric field is strong enough to generate a conducting phase within an insulator. Lightning is the best known version of this phenomenon. ii) The other example is concerned with the formation of dissolution patterns

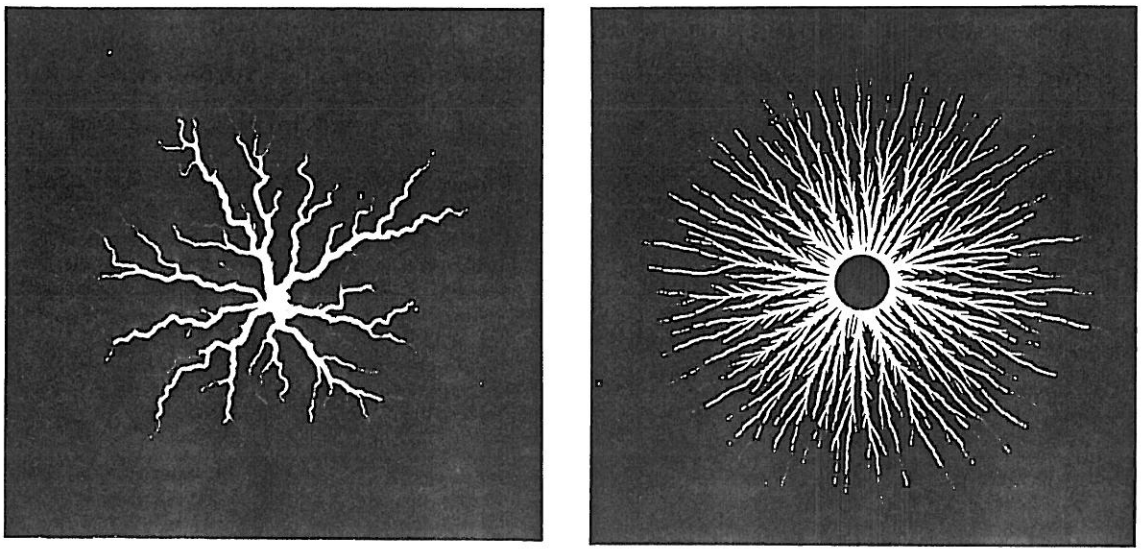

Figure 10.15. Time-integrated images of dielectric breakdown patterns. (a) Fractal structure obtained in a quasi-three-dimensional experiment (Niemeyer *et al* 1984) and (b) a dense branching structure observed under two-dimensional boundary conditions (courtesy of N. Allen).

in a porous medium. The nature of these experiments allows one to produce three dimensional objects which can be preserved for later studies of their fractal properties.

i) Fractal *dielectric breakdown* patterns can be studied by inducing a two dimensional radial discharge. To obtain a leader surface discharge (Lichtenberg figure) one can use the following arrangement (Niemeyer *et al* 1984). A starter electrode is brought into contact with an insulating (glass) plate. The other side of the plate is covered by a grounded conducting material, and the whole system is kept in compressed SF_6 gas of pressure 0.3 MPa. Applying a voltage pulse $30\text{kV}\times 1\mu\text{s}$ at the starter electrode a propagating discharge pattern can be observed. Fig. 10.15a shows a typical time-integrated image of such structures.

To estimate the fractal dimension of the pattern displayed in Fig. 10.15a one counts the number of branches $n(r)$ at a given distance from the centre. For a fractal of dimension D this number should scale as $n(r) \sim$

$dN(r)/dr \sim r^{D-1}$, where $N(r)$ is the total length of all branches (or the area measured with a given resolution) inside a circle of radius r. The branches are supposed to be extremely thin, and their thickness does not grow with the size of the object. (The apparent thickening of the branches in Fig. 10.15 is just an optical effect which is due to the number of carriers that have passed through a given branch.) In fact, there are more branches visible on the original negative, because the thinnest ones are lost in the course of reproduction. A careful counting of $n(r)$ suggests a value $D \simeq 1.7$ (Niemeyer *et al* 1984) in agreement with the dielectric breakdown model for $\eta = 1$ (Section 6.3.).

The physics of dielectric breakdown is quite complicated. During the growth of a discharge pattern a conducting phase is created as the interface advances. The channels consist of non-equilibrium plasma with mobile electrons produced by a critical electric field $\vec{\mathbf{E}}_c$ through electron impact ionization. The phenomenon can be described by the standard equation of electrodynamics: $-\nabla^2\phi = Q$ and $\vec{\mathbf{E}} = -\nabla\phi$, where ϕ is the electric potential and $Q = e\sum_{k,\sigma} \sigma n_k(\sigma)$ is the density of total charge with $n_k(\sigma)$ denoting the density of charge carriers of charge σ e. In the insulating phase Q is equal to zero, however, within the discharge pattern charge is created, annihilated and transported according to the expression

$$\partial n_k(\sigma)/\partial t = D_k(\sigma) n_k(\sigma), \tag{10.11}$$

where $D_k(\sigma)$ is a local but non-linear operator depending on $\vec{\mathbf{E}}$ and $n_k(\sigma)$. In the dielectric breakdown model (DBM) all the details represented by (10.11) are ignored by simply assuming that $\phi = Constant$ within the pattern. (This is a trivial solution of the Laplace equation for a conducting object.) Thus the charge density is assumed to be different from zero only at the interface, which is consistent with the observations. In addition to the above assumption, in the dielectric breakdown model the apparent stochasticity of the process is taken into account by selecting surface sites for occupation randomly.

In the original simulations of DBM it is assumed that the phenomenon

is essentially two-dimensional. Correspondingly, as a boundary condition for the potential (9.3) is used, i.e., ϕ is supposed to be constant along a large circle. However, the experiment is *quasi three-dimensional*, and the conducting material attached to the bottom of the glass plate provides a constant potential on the surface of a disc being at a small distance from the discharge in the third dimension. The simulations with $\eta = 1$ and boundary conditions corresponding to this situation resulted in nearly homogeneous clusters with a dimension close to 2 (Satpathy 1986). On the other hand, the fractal dimension of the simulated patterns agrees well with the experimental value if an exponent $\eta = 4$ is used in the calculation of the growth probabilities.

The complexity of the problem is further emphasized by Fig. 10.15b, where a discharge pattern obtained in a *two-dimensional experiment* (Allen 1986) is shown (with a circular electrode in the same plane with the pattern). In this case the structure seems to be dense ($D \simeq 2$) (Niemeyer *et al* 1986), while DBM gives $D \simeq 1.7$. Since on physical grounds one expects $\eta = 1$, one concludes that to make the DBM become a realistic model for dielectric breakdown a number of such additional effects have to be taken into account as the existence of a threshold field and the internal resistance of the plasma channels.

ii) *Chemical dissolution of a porous medium* involves the flow of a liquid in the medium coupled with a chemical reaction. In this sense the process is similar to viscous fingering in a random environment, with the difference that with the motion of the interface part of the medium is removed (dissolved). The main idea of the experiment (Daccord and Lenormand 1987, Daccord 1987) is based on the phenomenon that plaster (hydrated calcium sulfate) is slightly soluble in pure water.

The related investigations can be carried out in a *three-dimensional* sample with a characteristic linear size ~ 5 cm. The plaster is prepared by mixing 10 parts of pure water with 11 parts of $CaSO_4 \cdot 0.5H_2O$. Initially the sample is saturated with water so that the system is in chemical equilibrium. Then pure water is pumped through one of the faces at a constant rate, displacing the saturated water and subsequently dissolving some of the plaster. The resulting three-dimensional dissolution pattern is displayed in Fig.

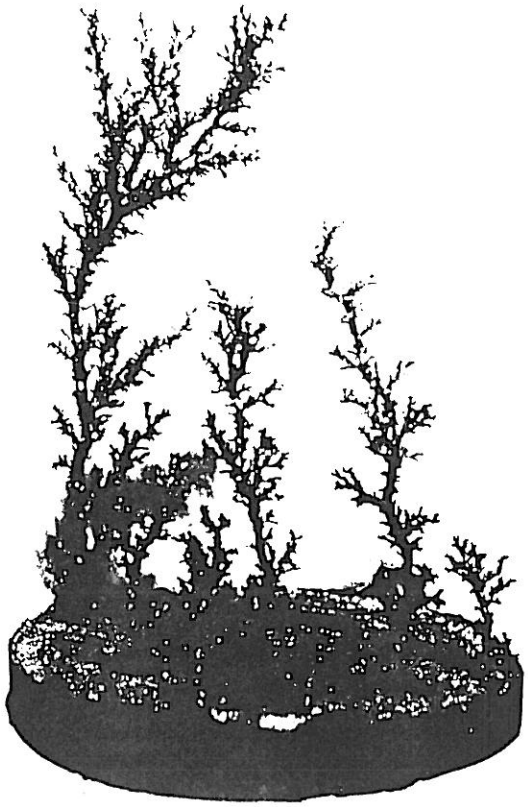

Figure 10.16. Three-dimensional trees obtained at the end of an experiment on chemical dissolution. These structures are made of Wood's metal which was used to fill the channels previously etched by water injected into plaster (Daccord and Lenormand 1987).

10.16 which is obtained by the following method. The channels etched by the water are filled with melted Wood's metal, and after cooling the plaster is completely dissolved.

The structure shown in Fig. 10.16 (and those obtained in the two-dimensional version of the experiment) reminiscent of the geometry of DLA clusters. To interpret this analogy one notes that the process of chemical dissolution shares many features with viscous fingering in a porous medium which, together with DLA, is governed by the Laplace equation. In ordinary viscous fingering there is a sharp increase in the viscosity (mobility) at the interface due to the high viscosity ratio of the fluids, and the motion of the interface is determined by the pressure distribution in the more viscous phase. In the experiments on chemical dissolution the injected reactive fluid and the

saturating displaced fluid has the same viscosity. However, at the interface (the reactive front), the permeability jumps from a low value in the porous medium to a much larger value in the etched channels. This corresponds to a considerable change in the effective viscosities. The randomness of the medium is provided by the porous structure of the plaster.

At places with high pressure gradient the flow is faster. In these regions the dissolution of plaster is more effective (its rate is proportional to the amount of incoming pure water), thus the geometry of the network of channels follows the flow of injected water. The effects of injection rate are rather complex in this experiment, but can be taken into account by appropriate rules in the related computer simulations (Daccord 1987).

It is far from trivial to give a reliable estimate for the fractal dimension of the obtained three-dimensional macroscopic objects. One possibility is to cut out quasi two-dimensional sections from the structure and evaluate the digitized image of these cross-sections. This procedure destroys the pattern. An alternative method based on capillary effects has recently been suggested to determine D for the type of objects produced by chemical dissolution.

The principle of the technique (Lenormand *et al* 1987) is to cover the fractal with a layer of *wetting fluid.* The structure is first immersed into the wetting fluid and next slowly lowered into a non-wetting one. Because of capillary effects the wetting fluid remains around the object. The characteristic radius of curvature R of the interface between the two fluids is determined by a balance between capillary and hydrostatic pressures. To evaluate the fractal dimension one needs to measure the volume of the wetting fluid $V(R)$ for various R. This can be achieved by using different pairs of fluids. Then the fractal dimension is obtained using the expression $V(R) \sim R^{3-D}$ which is the same as Eq. (4.9). Application of this method gives an estimate $D \simeq 1.8$ for the dimension of the dissolution patterns obtained by drilling a thin tube into the original sample and injecting the water radially from this central hole.

With the two examples presented in this Section we close the discussion of phenomena related to fractal growth governed by the Laplace equation.

Of course, there are numerous further growth processes leading to fractal structures. Many of these involve mechanisms which are related to, but are more complex than those reviewed in the present Part. Some of the *biological patterns* (trees, roots, blood vessels) (Mandelbrot 1982) or *networks of cracks* (Louis and Guinea 1987) in solids can be regarded as examples for growing fractals as well.

REFERENCES (PART III)

Alexander, S., Bruinsma, R., Hilfer, R., Deutscher, G. and Lereah Y., 1988 *Phys. Rev. Lett.* **60**, 1514

Ben-Jacob, E., Godbey, Y., Goldenfeld, N. D., Koplik, J., Levine, H., Mueller, T., and Sander, L. M., 1985 *Phys. Rev. Lett.* **55**, 1315

Ben-Jacob, E., Deutscher, G., Garik, P., Goldenfeld, N., and Lereah, Y., 1986 *Phys. Rev. Lett.* **57**, 1903

Bensimon, D., Kadanoff, L. P., Liang, S., Shraiman, B. I., and Tang, L., 1986 *Rev. Mod. Phys.* **58**, 977

Brady, R. M. and Ball, R. C., 1984 *Nature* **309**, 225

Buka, A., Kertész, J. Vicsek, T., 1986 *Nature*, **323**, 424

Buka, A., Palffy-Muhoray, P. and Rácz, Z., 1987 *Phys. Rev.* **A36**, 3984

Chen, J. D. and Wilkinson, D., 1985 *Phys. Rev. Lett.* **55**, 1982

Clément, E., Baudet, C. and Hulin, J. P., 1985 *J. Physique Lett.* **46**, L1163

Couder, Y., Cardoso, O., Dupuy, D., Tavernier, P. and Thom, W., 1986 *Europhys. Lett.* **2**, 437

Couder, Y., Gerard, N. and Rabaud, N., 1986 *Phys. Rev.* **A34**, 5175

Daccord, G., Nittmann, J., and Stanley, H. E., 1986 *Phys.Rev. Lett.* **56**, 336

Daccord, G., 1987 *Phys. Rev. Lett.* **58**, 479

Daccord, G. and Lenormand, R., 1987 *Nature* **325**, 41

DeGregoria, A. J. and Schwartz, L. W., 1986 *J. Fluid. Mech.* **164**, 383

DeGregoria, A. J. and Schwartz, L. M., 1987 *Phys. Rev. Lett.* **58**, 1742

Elam, W. T., Wolf, S. A., Sprague, J., Gubser, D. U., Van Vechten, D., Barz, G. L. and Meakin, P., 1985 *Phys. Rev. Lett.* **54**, 701

Family, F., Platt, D. and Vicsek, T., 1987 *J. Phys.* **A20**, L1177

Goldenfeld, N., 1988 *Phys. Rev.* **A37**,

Grier, D. G., Kessler, D. A. and Sander, L. M., 1987 *Phys. Rev. Lett.* **59**, 2315

Grier, D., Ben-Jacob, E., Clarke, R., and Sander, L. M., 1986 *Phys. Rev. Lett.* **56**, 1264

Hele-Shaw, J. S. S., 1898 *Nature* **58**, 34

Honjo, H., Ohta, S. and Matsushita, M., 1986 *J. Phys. Soc. Japan* **55**, 2487

Horváth, V., Vicsek, T. and Kertész, J., 1987 *Phys. Rev.* **A35**, 2353

Horváth, V., Kertész, J. and Vicsek, T., 1987 *Europhys. Lett.* **4**, 1133

Kadanoff, L. P., 1985 *J. Stat. Phys.* **39**, 267

Kaufman, J. H., Nazzal, A. I., Melroy, O. R. and Kapitulnik, A., 1987 *Phys. Rev.* **B35**, 1881

Kertész, J., and Vicsek, T., 1986 J. Phys. **A19**, L257

Kertész, J., Vicsek, T. and Meakin, P., 1986 *Phys. Rev. Lett.* **57**, 3303

Kessler, A., Koplik, J. and Levine, H., 1984 *Phys. Rev.* **A30**, 2820

Kessler, D. A., Koplik, J. and Levine, H., 1987 in *Patterns, Defects and Microstructures in Nonequilibrium Systems* edited by D. Walgraef (Martinus Nijhoff, Dordrecht)

Kessler, D. A., Koplik, J. and Levine, H., 1988 it Advances in Physics to appear

Langer, J. S., 1980 *Rev. Mod. Phys.* **52**, 1

Lenormand, R. and Zarcone, C., 1985 *Phys. Rev. Lett.* **54**, 2226

Lenormand, R., 1986 *Physica* **140A**, 114

Lenormand, R., Soucémarianadin, A., Tourboul, E. and Daccord, G., 1987 *Phys. Rev.* **A36**, 1855

Liang, S., 1986 *Phys. Rev.* **A33**, 2663

Liu, B. X., Huang, L. J., Tao, K., Shang, C. H. and Li, H. D., 1987 *Phys. Rev. Lett.* **59**, 745

Louis, E. and Guinea, F., 1987 *Europhys. Lett.*, **3**, 871

Maloy, K. J., Feder J. and Jossang, J., 1985 *Phys. Rev. Lett.* **55**, 2681

Mandelbrot, B. B., 1982 *The Fractal Geometry of Nature* (Freeman, San Francisco)

Matsushita, M., Sano, M., Hayakawa, Y., Honjo H. and Sawada, Y., 1984 *Phys. Rev. Lett.* **53**, 286

Matsushita, M., Hayakawa, Y. and Sawada, Y., 1985 *Phys. Rev.* **A32**, 3814

Meakin, P., Family, F. and Vicsek, T., 1987 *J. Colloid Interface Sci.* **117**, 394

Miller, A., Knoll, W. and Möhwald, H., 1986 *Phys. Rev. Lett.* **56**, 2633

Mullins, W. W. and Sekerka, R. F., 1963 *J. Appl. Phys.* **34**, 323

Niemeyer, L., Pietronero, L. and Wiesmann, H. J., 1984 *Phys. Rev. Lett.* **52**, 1033

Niemeyer, L., Pietronero, L. and Wiesmann, H. J., 1986 *Phys. Rev. Lett.* **57**, 650

Nittmann, J., Daccord, G., and Stanley, H. E., 1985 *Nature* **314**, 141

Nittmann, J. and Stanley, H. E., 1986 *Nature* **321**, 663

Nittmann, J. and Stanley, H. E., 1987 *J. Phys.* **A20**, L1184

Nittmann, J., Stanley, H. E., Touboul, E. and Daccord, G., 1987 *Phys. Rev. Lett.* **58**, 619

Ohta, S. and Honjo, H., 1988 *Phys. Rev. Lett.* **60**, 611

Oxaal, U., Murat, M., Borger, F., Aharony, A., Feder, J. and Jossang, T., 1987 *Nature* **329**, 32

Park, C. W. and Homsy, G. M., 1985 *Phys. Fluids* **28**, 1583

Paterson, L., 1981 *J. Fluid Mech.* **113**, 513

Paterson, L., 1984 *Phys. Rev. Lett.* **52**, 1621

Paterson, L., 1985 *Phys. Fluids* **28**, 26

Radnóczy, G., Vicsek, T., Sander, L. M. and Grier, D., 1987 *Phys. Rev.* **A35**, 4012

Ramanlal, P. and Sander, L. M., 1987 preprint

Rauseo, S. N., Barnes, P. D. and Maher, J. V., 1987 *Phys. Rev.* **A35**, 1245

Saffman, P. G. and Taylor, G. I., 1958 *Proc. Roy. Soc. London* Ser. **A245**, 312

Sander, L. M., Ramanlal, P. and Ben-Jacob, E., 1985 *Phys. Rev.* **A32**, 3160

Sarkar, S., 1985 *Phys. Rev.* **A32**, 3114

Sarkar, S. and Jasnow, D., 1987 *Phys. Rev.* **A35**, 4900

Satpathy, S., 1986 *Phys. Rev. Lett.* **57**, 649

Sawada, Y., 1986 *Physica* **140A**, 134

Sawada, Y., Dougherty, A., and Gollub, J. P., 1986 *Phys. Rev. Lett.* **56**, 1260

Stokes, J. P., and Weitz, D. A., Gollub, J. P., Dougherty, A., Robbins, M. O., Chaikin, P. M. and Lindsay, H. M., 1986 *Phys. Rev. Lett.* **57**, 1718

Szép, J., Cserti J. and Kertész J., 1985 *J. Phys.* **A18**, L413

Tabeling, P. and Libchaber, A., 1986 *Phys. Rev.* **A33**, 794

Tang, C., 1985 *Phys. Rev.* **A31**, 1977

Van Damme, H., Obrecht, F., Levitz, P., Gatineau, L. and Laroche, C., 1986 *Nature* **320**, 731

Vicsek, T., 1984 *Phys. Rev. Lett.* **53**, 2281

Vicsek, T., 1985 *Phys. Rev.* **A32**, 3084

Vicsek, T., 1987 *Physica Scripta*, **T19**, 334

Vicsek, T. and Kertész, J., 1988 *Europhys. News* **19**, 24

Witten, T. A. and Sander, L. M., 1983 *Phys. Rev.* **B27**, 5686